Grid Adaption and Its Effect on Entrainment in an *E–l* Model of the Atmospheric Boundary Layer

BRIAN H. FIEDLER

School of Meteorology, University of Oklahoma, Norman, Oklahoma

(Manuscript received 15 March 2001, in final form 23 August 2001)

ABSTRACT

A one-dimensional numerical model KOLUM is introduced that demonstrates the use of continuous dynamic grid adaption in modeling the atmospheric boundary layer. The entrainment rates of KOLUM are compared against recent calibrations for smoke clouds and water clouds derived from large-eddy simulations. The simulations performed with KOLUM support the claim that turbulent kinetic energy–diagnostic length scale (*E–l*) models overpredict entrainment by smoke and water clouds, independent of the use of grid adaption. The benefits of grid adaption are slight. Curiously, the simulations did not confirm spurious entrainment of *E–l* models in episodes of subsidence.

1. Introduction

A numerical model KOLUM is introduced that demonstrates the use of continuous dynamic grid adaption in modeling the atmospheric boundary layer. Continuous dynamic grid adaption means that the grid points continuously move either up or down to concentrate grid points where finer resolution is desirable. In the examples to be presented here, that will be in the entrainment zone at the top of the atmospheric boundary layer. Continuous dynamic grid adaption has been demonstrated for two- and three-dimensional flows in Fiedler and Trapp (1993) and Fiedler (1998). The one-dimensional implementation shown here is simpler than those efforts, and does not rely on the tensor formalism. Here, *grid adaption* will mean continuous dynamic grid adaption.

KOLUM is designed to retain the global conservation properties of the continuous equations. The inclusion of a scheme that allows for moving grid points is not difficult; a grid velocity appears as an additional factor in the advection terms. We do not claim the grid movement used here is optimal by a formal condition. Rather, we present a reasonable grid movement for these example cases, all of which have one obvious elevated zone requiring enhanced resolution.

The physics in KOLUM is simple. It is a turbulent kinetic energy–diagnostic length scale (*E–l*) model, not unlike Lenderink et al. (1999), but with the Bougeault and Lacarrère (1989) length scale. The very simple radiation schemes of Bretherton et al. (1999) and Moeng (2000) are used to investigate idealized situations. The primary purpose of KOLUM is to assess the advantages of grid adaption. The grid adaption does allow for numerical solutions to maintain sharper interfaces in the entrainment zone. However, we find that the entrainment rates for the simulated clear, smoky, and cloudy boundary layers are not significantly affected by a change from a 50-m resolution offered by a static grid, to the 20-m resolution provided by grid adaption. We are not able to make the case that software development resources of operational forecast centers would be best spent on implementing this grid adaption into numerical models, as opposed to, say, improving vertical advection schemes.

Nevertheless, the development of KOLUM presented an opportunity to use the recent large-eddy simulation–derived calibrations of smoke clouds (Bretherton et al. 1999) and water clouds (Moeng 2000), and to thus address some issues independent of grid adaption. KOLUM is tuned to produce the widely accepted calibration for a clear, convective boundary layer: the entrainment buoyancy flux should be 20% of the surface buoyancy flux. Having been so constrained, KOLUM produces excessive entrainment for a smoke cloud, as would be expected for an *E–l* model according to the analysis of Lenderink et al. (1999). Similarly, KOLUM produces excessive entrainment for water clouds. Curiously, KOLUM does not produce spurious numerical entrainment during subsidence episodes, as did the *E–l* model of Lenderink and Holtslag (2000).

A brief overview of the model is presented in section 2. Section 3 describes the details of the scheme that moves the grid points, followed by a demonstration with

Corresponding author address: Dr. Brian Fiedler, School of Meteorology, EC 1310, 100 E. Boyd St., Norman, OK 73019.
E-mail: bfiedler@ou.edu

wave motion in section 4. Sections 5–7 apply KOLUM to clear, smoky, and cloudy boundary layers.

2. Model description

KOLUM is an *E–l* model similar to that described in Lenderink and Holtslag (2000). Quantities diffuse in the vertical, down the gradient, with a diffusivity that is calculated from a prognosticated turbulent kinetic energy E. The virtual potential temperature flux in saturated conditions, which is one of the terms that produce E, is as described in Cuijpers and Duynkerke (1993). Subsidence and divergence of the horizontal wind are accomodated in the model.

KOLUM has the following differences from the *E–l* model of Lenderink and Holtslag (2000). The turbulent length scale $\lambda(z)$ is predicted with the nonlocal integrals as in Bougeault and Lacarrère (1989). At a given elevation z, λ is calculated as the geometric mean of two length scales: the distances a parcel could travel adiabatically upward and downward against (with) the work of buoyancy if all the turbulent kinetic energy were converted to gravitational potential energy. The dissipation rate of turbulent kinetic energy E is assumed to be

$$\frac{\alpha_E}{\lambda} E^{3/2}. \tag{1}$$

The diffusivity for all quantities, including E, is assumed to be

$$K = \alpha_K \lambda \sqrt{2E}. \tag{2}$$

The constants α_E and α_K are tuned in the experiments mentioned later.

KOLUM is not Boussinesq. The vertical coordinate is a mass coordinate, or equivalently, a hydrostatic pressure coordinate. A grid adaption, or grid movement, is naturally incorporated into the vertical advection term. The vertical advection has options for first- through third-order accuracy, as the flux forms listed in Tremback et al. (1987). Optionally, an additional monotonic correction can be added to the advection calculation.

3. The grid adaption

Turbulent kinetic energy E and turbulent fluxes (except of E) are calculated on levels with mass coordinate C_k, where k is an integer index. The other variables are also subscripted with an integer index. For example, m_k is the mass-coordinate interval between two flux levels:

$$m_k = C_{k+1} - C_k. \tag{3}$$

Let $\tilde{m}_k$ be the default grid interval in the absence of grid adaption. In section 4, these will be values that make the height interval about 50 m in the lowest 3.5 km of the atmosphere. But in subsequent adaptive simulations, $\tilde{m}_k$ will define a grid appropriate for a nocturnal boundary layer, representing an extreme case of concentrating the resolution near the ground (e.g., the left of Fig. 3).

The grid adapts by specifying desired grid intervals m_k^{n+1} at time t^{n+1} relative to the magnitude of the default $\tilde{m}_k$:

$$m_k^{n+1} = \beta^n f(z_k^n, h^n)\tilde{m}_k. \tag{4}$$

Here

$$\beta^n = \frac{\sum \tilde{m}_k}{\sum f(z_k^n, h^n)\tilde{m}_k} \tag{5}$$

and h^n is a diagnosed height of the boundary layer top at time t^n. The role of β^n is to enforce

$$\sum m_k = \sum \tilde{m}_k. \tag{6}$$

The following remarks apply for values of $\tilde{m}_k$ chosen to place high resolution in the nocturnal boundary layer. The weighting function f is also a function of some tunable parameters, as well as the variables z_k and h. When h is less than a specified threshold value $\tilde{h}$, f is kept at unity. As the boundary layer deepens, f is made greater than unity in what was the nocturnal boundary layer, and less than unity above $\tilde{h}$, but below h. Also, f is further reduced in a region of several hundred meters surrounding h^n. Thus, as a boundary layer deepens, KOLUM sacrifices resolution near the ground to provide resolution throughout the boundary layer and especially at the boundary layer top. The adaption is designed to produce little change in C_k above the boundary layer as a result of the adaption happening in and near the boundary layer.

The first-order, time-integration scheme we employ in the model allows for us to simply use

$$\frac{dC_k^n}{dt} = \frac{C_k^{n+1} - C_k^n}{t^{n+1} - t^n} \tag{7}$$

in the factor that appears in the advection term.

4. A wave test

Here we test the grid adaption for a situation that has the appearance of waves traveling on a smoke-filled boundary layer. We set $K = 0$. The intent is to test the accuracy of both the advection scheme and the grid adaption scheme at the sharp interface between the smoky and clear air, the height of which defines h. A vertical mass flux is specified as proportional to $P(z)\cos\omega t$ where $P(z)$ is chosen to be zero at the top and bottom, and peak in magnitude at $z = 1500$ m, which is also the initial height of the smoke interface. In all simulations the time step is 10 s.

Figure 1 shows a time–height cross section of the simulation using third-order, upwind advection with the monotonic correction. The grid interval is approximately 20 m near the smoke interface. The grid adaption produces very little movement of the grid away from

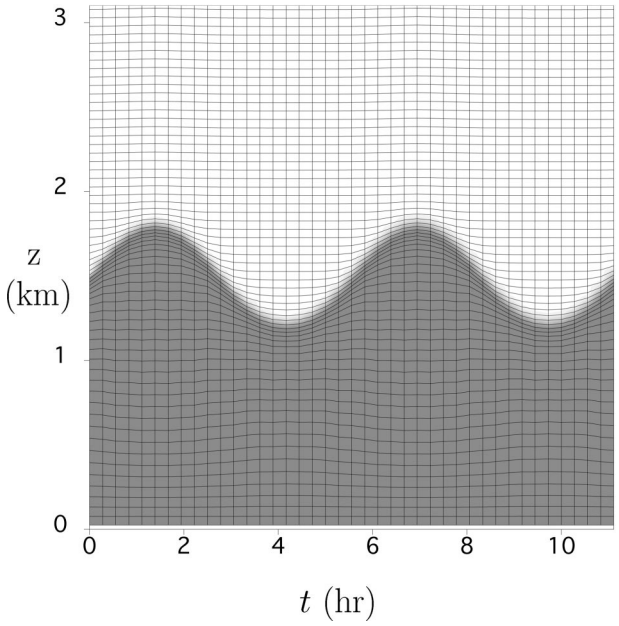

FIG. 1. Test of the grid adaption scheme with an imposed periodic vertical motion field, resembling that of a wave. Smoke as a function of z and t, and the grid. Turbulent mixing is turned off.

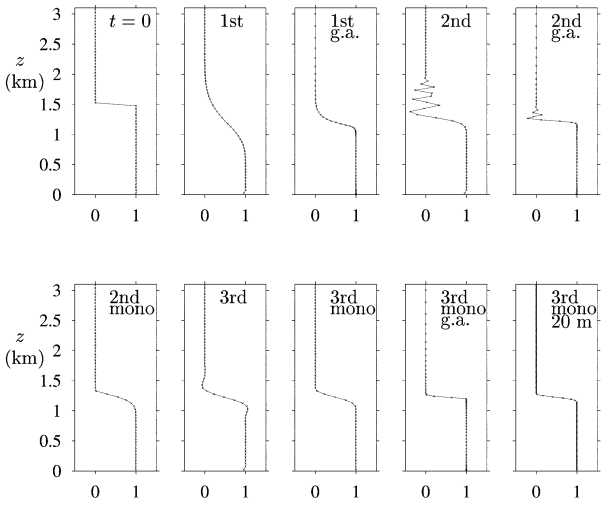

FIG. 2. A test of a various advection schemes and grid adaption schemes within KOLUM for a simulation as in Fig. 1. The profile of smoke at $t = 9.72$ h (a trough in the wave) is shown. The order of the scheme is indicated (1st, 2d, 3d). Here, g.a. means with grid adaption, mono means with the monotonic correction, and 20 m is a higher resolution static-grid simulation, as described in the text. The 3d mono g.a. is what was used in Fig. 1.

the zone of grid adaption. This is considered to be a favorable design feature.

The profile of smoke at the time of the final trough, or $t = 9.72$ h, is shown in Fig. 2 and compared with eight other advection and grid schemes. Except for one, all the simulations model 18 km of atmosphere with 90 grid points. Five of the static grids are stretched to put a 50-m grid interval in the lowest 3.5 km. One of the static grid simulations uses 180 points, statically stretched to provided a grid interval of 20 m in the lowest 3.5 km. The first-order scheme is highly diffusive and the second-order scheme produces large, erroneous oscillations: as is well known, it is inadvisable to use such schemes. The third-order scheme, and the monotonic one in particular, are better choices. The smoke interface is initialized across one grid point. With a static grid, the third-order monotonic scheme spreads the interface across four grid intervals, whether the grid interval is 50 m or 20 m. The use of grid adaption spreads the interface across three intervals. So not only does grid adaption conserve computational resources as compared to a static grid with similar resolution, but also the grid adaption reduces numerical diffusion in the simulation because of the tendency for grid points to follow the interface. The grid adaption offers some modest improvement in the numerical solution. The improvement can be substantial with the use of low-order advection schemes, but that seems a rather unlikely circumstance for a well-designed model. We now turn to elucidating any practical consequences of this numerical improvement. The subsequent simulations in this paper use the third-order monotonic scheme with 90 grid points (unless otherwise noted) in the troposphere, with or without grid adaption.

5. Test of a clear convective boundary

Here we model a boundary layer heated from below with a turbulent flux of potential temperature $F_\theta = 0.1$ kg K m^{-2} s^{-1}. The surface pressure is 10^5 Pa. The initial height is $h = 150$ m, which is just outside the specified $\tilde{h} = 75$ m. In Fig. 3 we see a concentrated zone of grid points following $h(t)$, which is diagnosed from the sharp temperature gradients. (At the initial time $h > \tilde{h}$ so the grid is shown lifted somewhat from the default nocturnal grid.)

Profiles of quantities in the deepening boundary are shown in Fig. 4. In a similar simulation in Cuxart et al. (2000), we see a maximum E of 1.1 m^2 s^{-2} when the boundary layer is 1 km deep, as it is here at 2×10^4 s. If we use $\alpha_E = 0.25$, the maximum value would be 1.58 m^2 s^{-2}. If we use $\alpha_E = 0.75$, the maximum value would be 0.89 m^2 s^{-2}. Hence the decision was made to use $\alpha_E = 0.5$. In a simulation with a uniform $\Delta z \approx 50$ m, plots of profiles appear indistinguishable from those in Fig. 4.

The minimum value of the turbulent flux of virtual potential temperature $F_{\theta_v}(z)$, for simulations with and without grid adaption, is shown in Fig. 5 as a function of time. Using grid adaption reduces transient effects of the entrainment of grid points. After 5 h, both simulations maintain, on average, $\min(F_{\theta_v}) = -0.023$ kg K m^{-2} s^{-1}, and the transients have no consequence on the net evolution of the boundary layer. The same statement can also be made about a simulation for which

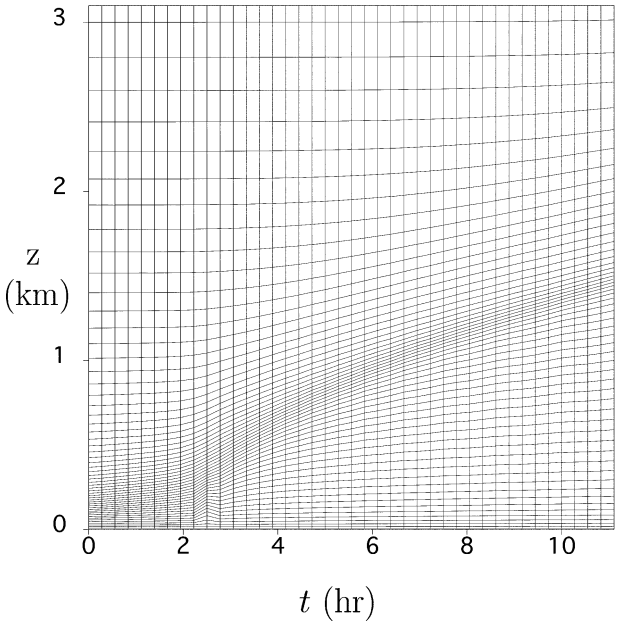

FIG. 3. Grid in the simulation of the deepening, clear, convective boundary layer.

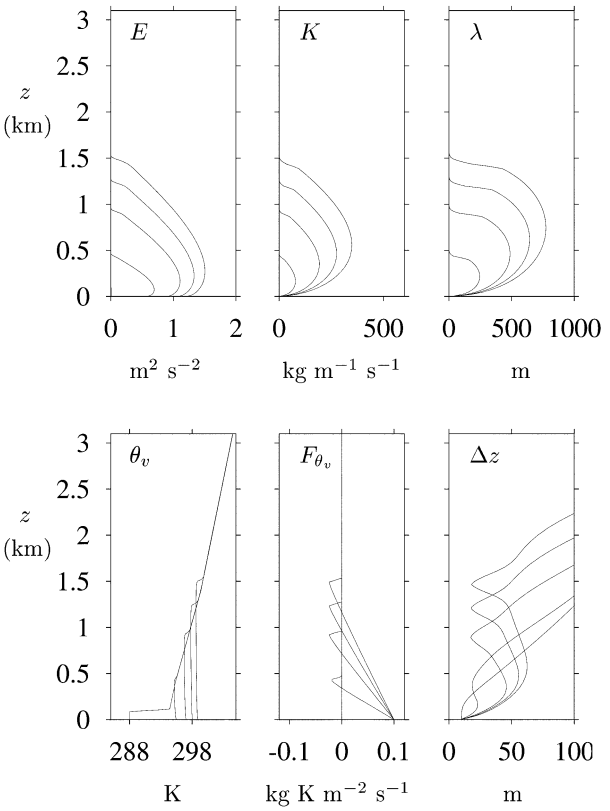

FIG. 4. A clear convective boundary layer with an imposed surface heat flux, using the adaptive grid. Profiles are plotted every 10^4 s out to 4×10^4 s. (The profiles deepen monotonically with time, and so are not labeled.)

$\Delta z = 100$ m (not shown). We will not find much need for grid adaption if modeling a clear, convective boundary layer is the only goal of our models.

If we use $\alpha_K = 0.125$, then $\min(F_{\theta_v}) \approx -0.15$. If $\alpha_K = 0.375$, then $\min(F_{\theta_v}) \approx -0.31$. We choose to use $\alpha_K = 0.25$ to keep the minimum entrainment flux to be about -20% of the surface buoyancy flux. Lenderink et al. (1999) also tune their *E–l* model, though with a different coefficient, to satisfy this 20% rule.

6. Test of a smoke-filled boundary layer

Here we apply the GEWEX Cloud Systems Study (GCSS) smoke test (Bretherton et al. 1999). The ''smoke'' concentration is initialized to a value of 1.0 in the boundary layer, and 0 aloft. The test is based on easily coded radiative cooling of an idealized smoke-filled boundary layer. Indeed, the purpose of the test is to isolate the modeling of turbulence from issues in modeling microphysics and radiation.

Bretherton et al. (1999) present models integrated out to 3 h, with many plots and statistics averaged over the third hour. KOLUM is, of course, trivially cheap compared to an LES, and a longer integration allows for a clearer difference between the beginning and final fields. Here, we integrate out to 4×10^4 s, or 11 h. Figure 6 shows the profiles of simulations with a grid adaption that maintains $\Delta z \approx 20$ m in the entrainment zone. Profiles from simulations without grid adaption, with $\Delta z \approx 50$ m, are virtually indistinguishable.

The fundamental result of Bretherton et al. (1999) is that the high-resolution 3D codes all had between 22 W m^{-2} and 30 W m^{-2} upward heat flux into the ''cooling zone'' at the top of the boundary layer. This means that there was an entrainment heat flux of about -30 W m^{-2}, in a sense ''offsetting'' half of the 60 W m^{-2} radiative heat flux at cloud top. In Fig. 6 we see only about 12 W m^{-2} into cloud base, indicating an entrainment heat flux of -48 W m^{-2}. Lenderink et al. (1999) also show how *E–l* models are expected to produce a greater entrainment flux than a model that resolves the eddies. They show that *E–l* models should have an entrainment heat flux equal to the radiative heat flux in the limit of a thin cooling zone at cloud top. Indeed, Bretherton et al. (1999) show this characteristic for the one-dimensional models, the upward heat flux into the cooling layer is between 8 W m^{-2} and 15 W m^{-2}, indicating an entrainment heat flux of between 52 W m^{-2} and 45 W m^{-2}, for a 60 W m^{-2} radiative heat flux at cloud top.

Figure 7 shows the maximum value of the turbulent flux of smoke F_s as a function of time, both with and without grid adaption. Both simulations suffer from ''gridpoint events'' as the interface passes through a grid point. The time-average of these events is evidently nearly the same for both schemes, given the nearly identical net evolution of the boundary layer.

KOLUM locates h by using a parabolic fit to inter-

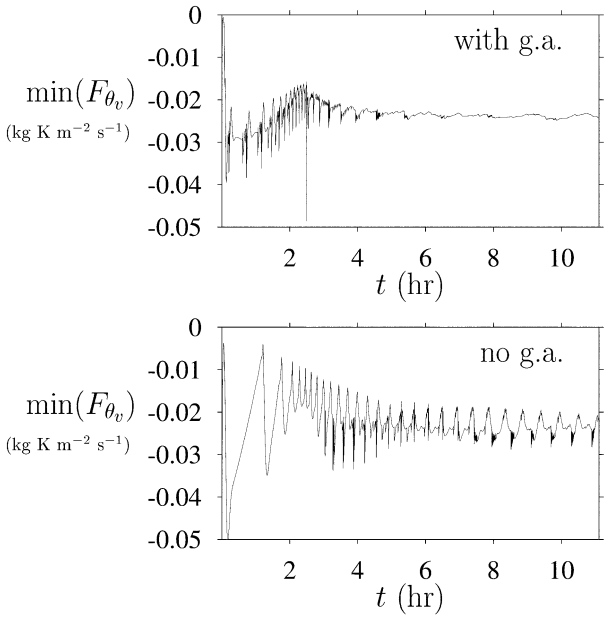

FIG. 5. Values of min(F_{θ_v}) in the clear convective boundary layer simulation, with and without grid adaption (g.a.).

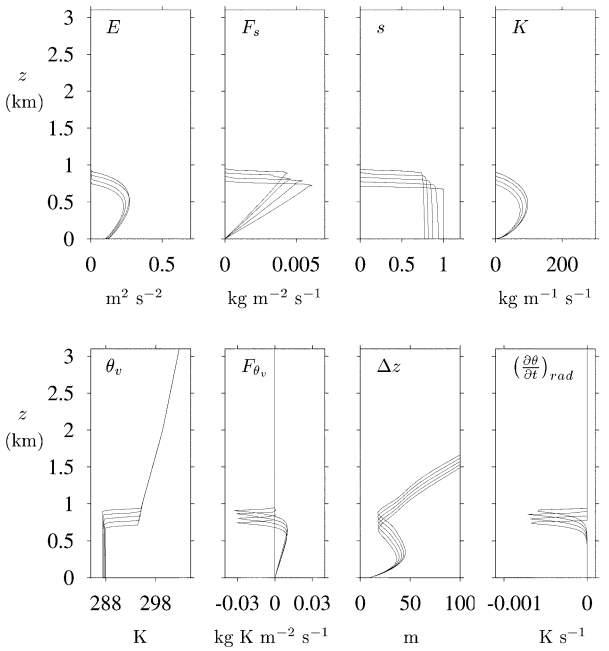

FIG. 6. A test of the smoke-filled boundary layer, using the adaptive grid. Profiles are plotted every 10^4 s out to 4×10^4 s. (The profiles deepen monotonically with time, and so are not labeled.)

polate to the location of the maximum value of $\partial s/\partial z$. In all simulations, $h(t)$ rises very smoothly with time. With grid adaption, the net rise is 221 m ($w_e = 0.0055$ m s^{-1}); with $\Delta z = 50$ m, the rise is 244 m ($w_e = 0.0061$ m s^{-1}). Reducing the total number of grid points to 45 and using $\Delta z = 100$ m results in a rise of 251 m ($w_e = 0.0063$ m s^{-1}).

The standard radiation absorption coefficient was increased by a factor of 10 in an attempt to design a more brutal test for the grid. With that increase, the radiative cooling is concentrated in nearly one grid point on cloud top: with $(\partial\theta/\partial t)_{\text{rad}} = -0.0024$ K s^{-1} for the adaptive grid and $(\partial\theta/\partial t)_{\text{rad}} = -0.0008$ K s^{-1} for the static grid. With grid adaption the rise is 296.3 m; with a static grid the rise is 296.7 m. As was also experienced with the clear convective boundary layer, simulations of the smoke-filled boundary layer do not benefit much from grid adaption.

Last, we use the smoky boundary layer to test for a potential problem that was presented by Lenderink and Holtslag (2000). They showed an *E–l* scheme for which subsidence could not properly advect the entrainment zone downward through grid points. Their scheme, in effect, adds a spurious entrainment rate to counteract the subsidence. However, Fig. 8 shows that this is not a universal problem with *E–l* models.

We add the wave motion and use a static grid, thus giving the simulation ample opportunity to suffer errors during subsidence. Yet the ultimate depth of the boundary layer is nearly the same as the simulation with no waves and with grid adaption. In their cloud-topped boundary layer simulation, Lenderink and Holtslag (2000) showed an effective entrainment rate increased by a factor of 3 during subsidence. We find insignificant spurious entrainment during subsidence.

In order to further investigate why we did not find spurious subsidence, we conduct an experiment much closer in design to that of Lenderink and Holtslag (2000). A divergence of the horizontal wind field is specified to be 6.67×10^{-6} s^{-1} below $z = 1500$ m. This puts a vertical velocity of $w = -0.005$ m s^{-1} at $z = 750$ m. In principle, this subsidence should compensate for the entrainment rate that would occur in the absence of subsidence, which was diagnosed to be $w_e \approx 0.005$ m s^{-1}, with or without grid adaption. In practice we find what happens in principle: the subsidence balances the entrainment, producing no change in the height of the inversion.

When the divergence of the horizontal wind is doubled, to 1.33×10^{-5} s^{-1}, we find the boundary layer height decreases by 150 m, to $z = 500$ m. The subsidence velocity minus the entrainment velocity would have varied linearly from approximately 0.005 m s^{-1} at $z = 750$ m to approximately 0.003 m s^{-1} at $z = 500$ m. An average rate of decrease in the height of the boundary layer of 0.004 m s^{-1} would have given a decrease of 160 m in 4×10^4 s, very close to what actually happened in the simulation. We conclude that, in modeling subsidence, the discrete, numerical scheme is faithful to the continuous equations.

Most curiously, the identical result also happens when KOLUM is modified to use the *E–l* scheme of Lenderink and Holtslag (2000) with first-order advection; it is this experiment that is shown in Fig. 8c. For the record, we

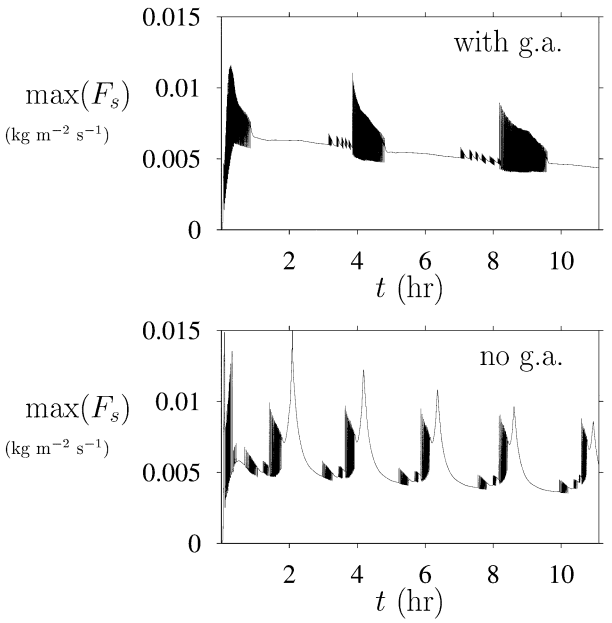

FIG. 7. The maximum value of F_s in simulations of the smoke-filled boundary layer, both with and without grid adaption (g.a.). The black areas result from episodes of somewhat irregular square-wave oscillations with period of approximately $6\Delta t$. Similar oscillations also occur with a time step reduced to $\Delta t = 1$ s.

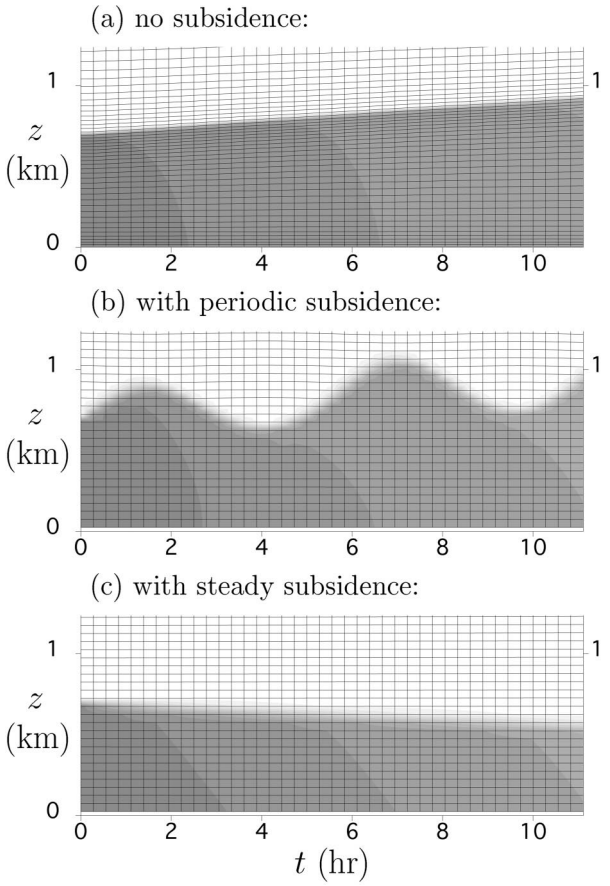

FIG. 8. A test for numerical errors associated with subsidence through grid points; (a) no subsidence, (b) periodic subsidence, and (c) steady subsidence. In this smoky boundary layer simulation, such subsidence associated with the imposed wave does not cause spurious entrainment. The steady subsidence test is computed with KOLUM modified to be as close as possible to Lenderink (2000), though the standard KOLUM produces nearly the same result.

also report that Fig. 8b is also nearly the same when the scheme of Lenderink and Holtslag (2000) is used for that simulation. Lenderink and Holtslag (2000) report that when they add subsidence to their smoke cloud experiments, the top of the boundary layer remains ''locked in'' to the grid of 25 m resolution, thus preventing the top of the boundary layer from advecting downwards. With 50 m resolution used here, the locked in effect should be worse, but it does not occur at all. If the locked in effect actually did occur, then grid adaption would be a good remedy. But, in these experiments, grid adaption is a solution looking for a problem.

7. Test of a cloudy boundary layer

Last, we test the effect of grid adaption in a simulation of a cloudy boundary layer. We do simulations similar to those of Moeng (2000). The initial conditions and the radiation parameterization are identical to Moeng (2000). Here, for simplicity, the surface fluxes of potential temperature and water vapor are set to a constant value: $F_\theta = 0.01$ kg K m^{-2} s^{-1} and $F_{q_v} = 1 \times 10^{-4}$ kg m^{-2} s^{-1}. Time–height cross sections of cloud water q_c and E are shown in Figs. 9 and 10. We find slightly more significant effects of the grid adaption, than we did with the smoke cloud. With grid adaption, the cloud remains thin but unbroken. Without grid adaption, the liquid water path is 13% less, and there is more variability in the cloud cover with time. However, this behavior does not appear to have any great consequence on the net entrainment. In both cases the entrainment rate is stabilized to a value that maintains marginal cloud cover. The stabilization to marginal cloud cover is clearly demonstrated by simulations with alternative values of F_{q_v} that are shown in Fig. 11. None of these simulations allow for thick cloud cover to develop, such a situation would increase entrainment and dry the boundary layer to again produce a marginal cloud cover. Likewise, none of these simulations allows for clouds to disappear for long: the resulting reduced entrainment allows for clouds to redevelop. Therefore, when intercomparing boundary layer schemes in this cloud-topped regime, we would expect very little difference in the modeled entrainment rate. The quantity of intercomparison should be the cloud amount that produced the entrainment.

The simulation in Fig. 9 entrains nearly 600 m, between $t = 1 \times 10^4$ s and $t = 4 \times 10^4$ s, giving an entrainment velocity of $w_e = 0.020$ m s^{-1}. The simulations maintains $\Delta\theta_l = 6$ K and, with grid adaption, an average liquid water path of 0.0144 kg m^{-2}, during

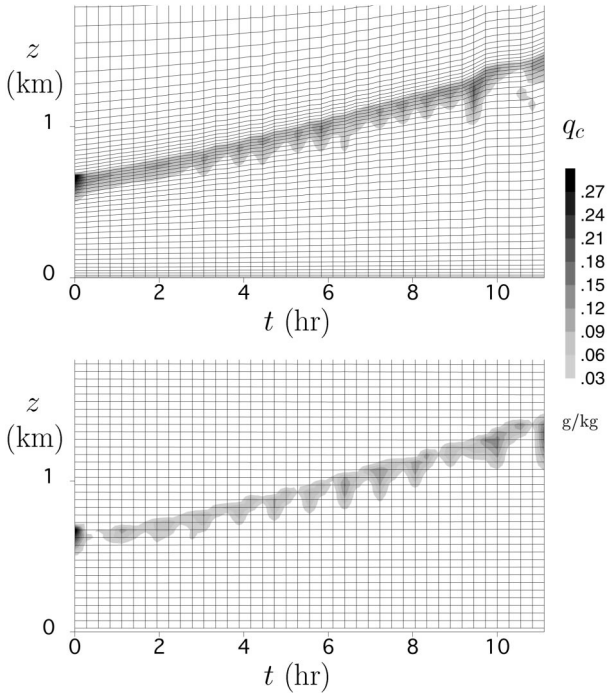

FIG. 9. Time–height cross section of liquid water q_c in the cloud-topped simulation, (top) with and (bottom) without grid adaption.

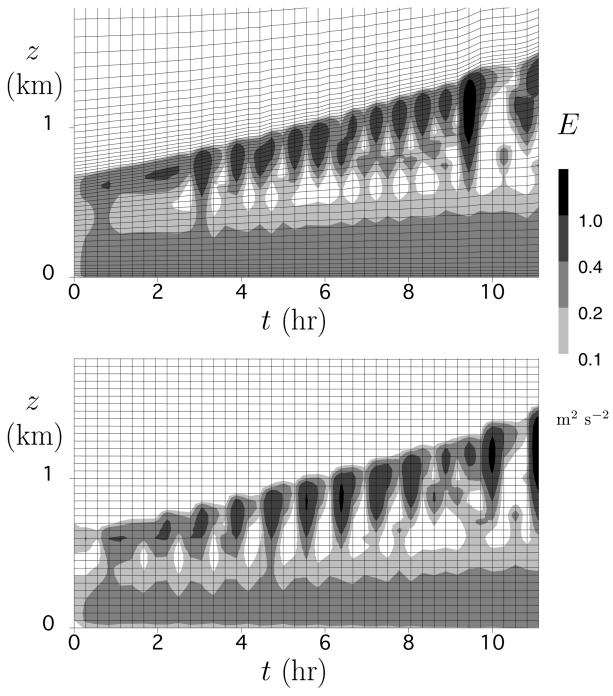

FIG. 10. Time–height cross section of turbulent kinetic energy E in the cloud-topped simulation, (top) with and (bottom) without grid adaption.

that time interval. Moeng (2000) offers a parameterization for entrainment velocity, based on large-eddy simulations. The parameterization is based on the surface buoyancy flux and radiation characteristics of the cloud, the latter of which are parameterized in terms of liquid water path. But the parameterization of Moeng (2000) would predict an entrainment velocity of $w_e = 0.0067\ \text{m s}^{-1}$, one-third the value that occured in our simulation.

The simulation with $F_{q_v} = 2 \times 10^{-5}\ \text{kg m}^{-2}\ \text{s}^{-1}$ shown in Fig. 11 has surface fluxes close to the regime studied by Moeng (2000). The net entrainment between $t = 1 \times 10^4$ s and $t = 4 \times 10^4$ s is 250 m, giving an entrainment velocity of $w_e = 0.0085\ \text{m s}^{-1}$. This simulation also maintains $\Delta\theta_l = 6$ K, but with an average liquid water path of $0.0062\ \text{kg m}^{-2}$. The parameterization of Moeng (2000) would predict $w_e = 0.0042\ \text{m s}^{-1}$, which is still less than one-half of what KOLUM did.

Thus, as compared with the parameterization of Moeng (2000), the cloudy boundary layer simulated by KOLUM produces excessive entrainment. There is no simple way to repair this by adjusting α_K downward. For example, using $\alpha_K = 0.125$ for the simulation in Fig. 9 produces a liquid path 2.5 times greater, but has insignificant effect on the entrainment rate, given that KOLUM tends to produce marginal cloud cover. The larger liquid water path increases the prediction of the Moeng (2000) parameterization to an entrainment velocity of $w_e = 0.0096\ \text{m s}^{-1}$ (from $w_e = 0.0067\ \text{m s}^{-1}$ predicted for the liquid water path produced with $\alpha_K =$

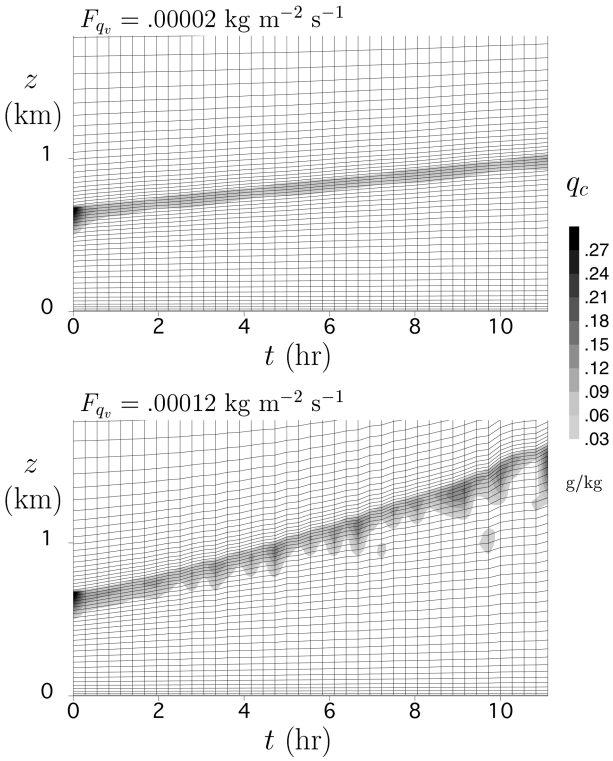

FIG. 11. Time–height cross section of liquid water q_c for simulations with the indicated alternative value of F_{q_v}.

0.25), thus reducing the discrepancy with the model value of $w_e = 0.020$ m s^{-1}. However, as mentioned in section 5, using $\alpha_K = 0.125$ would disrupt the good agreement with the widely accepted calibration for clear entrainment. The benefit would be only a small gain in performance towards the parameterization of Moeng (2000).

8. Conclusions

The model KOLUM has served to demonstrate a numerical scheme that adapts the vertical position of grid points. The testing of KOLUM has revealed little benefit for using such a scheme. The adaptive scheme, as used here, allowed for 20 m resolution in the entrainment zone while the static grid would provide 50 m. At least for that comparison, there were generally modest differences in the results. The differences would escape notice in an operational forecast. Obviously, more benefit may have been apparent if more extreme stretching was used with a fewer total number of grid points. In the entrainment zone, the static grid could then have been more coarse relative to the adaptive grid. However, such simulations often required repeated attempts at tuning the grid adaption for particular experiments. Needless to say, grid adaption with such performance would have little role to play in operational models.

However, the testing of KOLUM has served other purposes besides the testing of adaptive grid capabilities. With KOLUM having been constrained by design to faithfully simulate clear convective boundary layers, KOLUM overpredicted the entrainment rate caused by a smoke cloud by a factor of 2. This behavior confirms what was investigated in Lenderink et al. (1999), where it was shown that simple *E–l* models are expected to overpredict entrainment rates for a smoky boundary layer. Similarly, KOLUM simulations of a cloudy boundary layer produced an entrainment rate at least twice that of Moeng (2000). Last, we again mention that KOLUM did not show any problems of coping with downward subsidence of the entrainment zone, contrary to the experience of Lenderink and Holtslag (2000) with their *E–l* model.

The design for moving grid points in KOLUM required more careful consideration, and maintenance, of global conservation laws than is sometimes the case for boundary layer schemes in atmospheric models. However, the ultimate implementation of a reasonable adaptive grid scheme in one dimension was not difficult; grid movement is readily accounted for in vertical advection terms. With vertical advection being a fundamental component of KOLUM, a byproduct of this investigation was a demonstration of the importance of using accurate vertical advection in *E–l* models of the boundary layer. This is true whether the advection is caused either by moving grid points or by waves and subsidence.

Acknowledgements. This research was supported by the U.S. Department of Defense under Grant N00014-96-1-1112.

REFERENCES

Bougeault, P., and P. Lacarrère, 1989: Parameterization of orography-induced turbulence in a mesobeta-scale model. *Mon. Wea. Rev.,* **117,** 1872–1890.

Bretherton, C. S., and Coauthors, 1999: An intercomparison of radiatively driven entrainment and turbulence in a smoke cloud, as simulated by different numerical models. *Quart. J. Roy. Meteor. Soc.,* **125,** 391–423.

Cuijpers, J. W. M., and P. G. Duynkerke, 1993: Large eddy simulation of trade wind cumulus clouds. *J. Atmos. Sci.,* **50,** 3894–3908.

Cuxart, J., P. Bougeault, and J.-L. Redelsperger, 2000: A turbulence scheme allowing for mesoscale and large-eddy simulations. *Quart. J. Roy. Meteor. Soc.,* **126,** 1–30.

Fiedler, B. H., 1998: Continuous adaptation of a curvilinear grid. *Numerical Methods in Fluid Mechanics,* A. Vincent, Ed., CRM Proceedings and Lecture Notes, Vol. 16, American Mathematical Society, 99–107.

——, and R. J. Trapp, 1993: A fast dynamic grid adaption scheme for meteorological flows. *Mon. Wea. Rev.,* **121,** 2879–2888.

Lenderink, G., and A. A. M. Holtslag, 2000: Evaluation of the kinetic energy approach for modeling turbulent fluxes in stratocumulus. *J. Atmos. Sci.,* **57,** 244–258.

——, M. C. vanZanten, and P. G. Duynkerke, 1999: Can *E–l* turbulence closure simulate entrainment in radiatively driven convective boundary layers? *J. Atmos. Sci.,* **56,** 3331–3337.

Moeng, C.-H., 2000: Entrainment rate, cloud fraction, and liquid water path and PBL stratocumulus clouds. *J. Atmos. Sci.,* **57,** 3627–3643.

Tremback, C. J., J. Powell, W. R. Cotton, and R. A. Pielke, 1987: The forward-in-time upstream advection scheme: Extension to higher orders. *Mon. Wea. Rev.,* **115,** 540–554.